PAPER

Check for updates

Small chromium-doped silicon clusters $CrSi_n$: structures, IR spectra, charge effect, magnetism and chirality†

Bao-Ngan Nguyen-Ha, [ab] Ngoc Thach Pham,[c] Pieterjan Claes,[d] Peter Lievens, [d] André Fielicke, [e] Vu Thi Ngan,[c] Minh Tho Nguyen [*ab] and Ewald Janssens [*d]

A series of small chromium-doped silicon clusters $CrSi_n$ with n = 3–10 in the cationic, neutral and anionic charge states were investigated using quantum chemical methods. The $CrSi_n^+$ cations with n = 6–10 were produced in the gas phase and characterized by far-IR multiple photon dissociation (IR-MPD) spectroscopy. Good agreement between experimental spectra in the 200–600 cm^{-1} frequency range and those determined for the lowest-energy isomers by density functional theory calculations (B3P86/6-311+G(d)) provide a strong support for the geometrical assignments. An extensive structural comparison for the three different charge states shows that the structural growth mechanism inherently depends on the charge. While the structures of the cationic clusters are preferentially formed by addition of the Cr dopant to the corresponding pure silicon cluster, it favors substitution in both the neutral and anionic counterparts. The Si–Cr bonds of the studied $CrSi_n^{+/0/-}$ clusters are polar covalent. Apart from a basket-like $Cr@Si_9^-$ and an endohedral $Cr@Si_{10}^-$ cage, the Cr dopant takes an exohedral position and bears a large positive charge in the clusters. The exohedrally doped clusters also have a high spin density on Cr, manifesting the fact that the intrinsic magnetic moment of the transition metal dopant is well conserved. Three $CrSi_n$ clusters have a pair of enantiomeric isomers in their ground state, namely the cationic n = 9 and the neutral and anionic n = 7. Those can be distinguished from each other by their electronic circular dichroism spectra, calculated using time-dependent density functional theory. Those enantiomers, being intrinsically chiral inorganic compounds, might be used as building blocks of optical-magnetic nanomaterials because of their high magnetic moments and ability to rotate the plane of polarization.

[a] *Laboratory for Chemical Computation and Modeling, Institute for Computational Science and Artificial Intelligence, Van Lang University, Ho Chi Minh City, Vietnam. E-mail: ngan.nguyenhabao@vlu.edu.vn, minhtho.nguyen@vlu.edu.vn*

[b] *Faculty of Applied Technology, School of Technology, Van Lang University, Ho Chi Minh City, Vietnam*

[c] *Laboratory of Computational Chemistry and Modeling (LCCM), Department of Chemistry, Faculty of Natural Sciences, Quy Nhon University, Quy Nhon, Vietnam*

[d] *Quantum Solid State Physics, KU Leuven, Celestijnenlaan 200D, B-3001 Leuven, Belgium. E-mail: ewald.janssens@kuleuven.be*

[e] *Fritz-Haber-Institut der Max-Planck-Gesellschaft, Faradayweg 4-6, 14195 Berlin, Germany*

† Electronic supplementary information (ESI) available: (i) Structures and relative energies of the cationic, neutral and anionic $CrSi_n^{+/0/-}$ clusters (n = 3–10), (ii) average binding energies, fragmentation energies, ionization energies (IE$_a$), electron affinities (EA$_a$) and natural population analysis for ground states of $CrSi_n^{+/0/-}$ clusters, and (iii) calculated IR, UV-Vis and ECD spectra of low-lying enantiomers of $CrSi_n^{+/0/-}$ clusters. See DOI: https://doi.org/10.1039/d3cp00317e

1. Introduction

Miniaturization plays an important role in current technological developments, and attracts much attention in both fundamental research and industrial applications.[1] The demand of consumers for novel and cost-effective materials with salient, tailored properties has been, and still is, triggering an explosive advancement in the use of nanomaterials including assemblies of nanoparticles and small clusters. In this context silicon clusters have been studied extensively. However, due to the intrinsic dangling bonds,[2] the thermodynamic stability of pure silicon clusters turns out to be relatively low. Since the silicon atom favors sp^3 hybridization, pure silicon clusters exhibit geometries much different from their carbon analogues, and their inherent low stability means they are not usable as building blocks for nanomaterials.[3] Due to the peculiar properties of electrons in nd subshells, transition metal dopants can stabilize silicon clusters by fundamentally transforming their

geometric and electronic structures.[4] Of the 3d transition metals, chromium emerges as an interesting dopant thanks to its high magnetic moment caused by its half-filled 3d electron shell. This, for instance, has led to the use of Cr–Si alloys in resistors and microelectronic devices.[5–8]

The structures of several small and medium anionic $CrSi_n^-$ clusters were assigned by a combination of photoelectron spectroscopy and density functional theory (DFT) calculations. The magnetic moment of the Cr atom in $Cr@Si_{10}^-$ is proven to be quenched due to its encapsulation by a Si_{10} cage, whereas the stable exohedral geometries for $CrSi_n^-$ with $n = 3$–9 tend to exhibit significant magnetic moments ranging from 3 to $5\mu_B$.[9] The endohedral $Cr@Si_{14}^-$ anion in a doublet state with a C_{2v} geometry is the most stable cluster of the multiply Cr-doped $Cr_nSi_{15-n}^-$ $(n = 1$–3$)$ series, whereas the $Cr_2Si_{13}^-$ and the $Cr_3Si_{12}^-$ possess C_s and D_{6d} symmetric structures with magnetic moments of 3 and $7\mu_B$, respectively.[10] While the $CrSi_n^-$ anions with $n = 14$ and 15 exhibit fully endohedral structures, larger $CrSi_n^-$ $n = 16$–18 anions prefer a fullerene-type Si_{14} cage encapsulating a Cr atom, with the extra Si atoms added on the fullerene surface.[11] Due to the lack of experimental studies and dedicated computations, the structures and properties of neutral $CrSi_n$ and cationic $CrSi_n^+$ clusters are not yet well established, especially their magnetic moments and the size at which an exohedral–endohedral transition occurs.

Earlier studies of neutral $CrSi_n$ clusters, under a severe constraint of the lowest spin singlet state, claimed that a fully endohedral structure of $CrSi_n$ does not exist with $n < 12$.[9,12,13] The magic neutral $Cr@Si_{12}$ cluster was determined to have an endohedral hexagonal prism structure with a completely quenched magnetic moment.[14,15] This structure was also confirmed for the anionic $CrSi_{12}^-$ by photoelectron spectroscopic study (PES),[16] but the interpretation of its electronic properties has not reached a consensus yet.[14,17–19]

For the cations, Beck[20] conducted in 1987 the first experiments generating transition metal doped silicon cluster cages $M@Si_n$, with M = Cr, Mo, W, in a supersonic molecular beam[20] and drew a conclusion about a particular stability of the $Cr@Si_{15}^+$ and $Cr@Si_{16}^+$ cations,[21] which was confirmed in 2006 for related clusters by photofragmentation mass spectrometry experiments.[22] In another experiment using mass-selection in a time-of-flight mass spectrometer, the $Cr@Si_{15}^+$ and $Cr@Si_{16}^+$ clusters were reported that they dissociate *via* the loss of silicon, producing smaller Cr–Si species, enhancing for encapsulated Cr structures, whereas $CrSi_7^+$ prefers a primary loss of the Cr^+ ion and a neutral Si_7 unit, thus enhancing for an exohedral structure.[23] A Frank–Kasper polyhedral structure was suggested for the $Cr@Si_{16}^+$ cation based on X-ray absorption spectroscopy.[24] This $Cr@Si_{16}^+$ structure re-confirms and further points out that an occupied 1H state in the case of $Cr@Si_{16}^+$ compensates for the "non-magic" part within the spherical potential model; hence an electron shell closure is not a necessary condition to stabilize a cage-like structure as ground state.[25] $Cr@Si_{11}^+$ was identified as the smallest endohedral $CrSi_n^+$ cluster,[26] but the structures or smaller cationic $CrSi_n^+$ clusters are still elusive.

Previous joint experimental and computational studies using infrared multiple photon dissociation (IR-MPD) spectroscopy, far-infrared-vacuum-ultraviolet two color ionization spectroscopy, and DFT calculations have successfully assigned the geometrical structures of different metal clusters such as the Au clusters,[27–29] the recently discovered $NbAl_8H_8^+$ cluster,[30] cationic and neutral metal-doped silicon clusters $M@Si_n$ with Cu, V, Mn, Co, Ag, Au, Nb…[31–41] and pure cationic ($n = 6$–11, 13–15, 18)[42] and neutral Si_n ($n = 6$–10, 15)[43,44] clusters.

In the current work, a comprehensive analysis of cationic Cr-doped silicon clusters through experimental and computational methods is carried out. IR-MPD experiments are conducted on the $CrSi_n^+$ $n = 6$–10 cations, providing experimental benchmark data for the structural assignment of cationic Cr-doped silicon clusters. DFT computations are employed to investigate the electronic and geometric structures of cationic as well as neutral chromium doped silicon clusters for sizes $n = 3$–10. The anions, whose structures have already been experimentally and theoretically established in literature,[9] are re-optimized in this study at the same theoretical level as used for the cationic and neutral clusters, allowing a consistent comparison in energetic parameters, growth mechanisms, and other properties for all three charge states. In addition, this study reports the observation of chiral structures in some low-lying Cr-doped Si clusters. Although asymmetric geometries of clusters have been found in several studies by both experimental and theoretical methods alike,[45–52] they remain elusive until now,[53] especially chiral species with semiconductor relevance.[54] This finding motivates the investigation of the properties of chiral chromium-doped silicon clusters.

2. Methods

2.1 Experimental methods

All spectroscopic measurements are performed in a molecular beam setup[55] coupled to a beamline of the Free Electron Laser for Infrared experiments (FELIX) user facility.[56] The clusters are produced in a dual-target dual-laser vaporization cluster source by pulsed ablation of chromium and silicon plate targets. Cluster–argon complexes are formed by condensation of the vaporized material in a short pulse of He gas containing a fraction (5%) of Ar and cooled in a thermalization channel attached to the source (80 K). Cluster growth in such type of a gas aggregation source does not take place under thermal equilibrium conditions and kinetic trapping of structural isomers in local minima on the potential energy surface is possible.[57,58]

The experimental conditions (laser powers, gas pressure, timing) were optimized to produce silicon clusters containing 5–30 atoms with a low concentration of chromium (no or one chromium atom per cluster). Of these produced clusters, those with an exohedral Cr atom are found to absorb Ar most easily, *i.e.* $CrSi_n^+$ with $n = 6$–10.[26] It is on those Ar-tagged Cr-doped silicon clusters that the IR-MPD experiments are performed. A typical mass spectrum of $CrSi_n^+$ is presented in the ESI.†

This journal is © the Owner Societies 2023

Phys. Chem. Chem. Phys., 2023, **25**, 15340–15353 | **15341**

Resonant absorption of infrared light heats the cluster–argon complexes through internal vibrational redistribution, which may result in desorption of weakly bound Ar atoms from the complexes. Mass, and hence composition specific IR-MPD spectra are constructed by recording the mass spectrometric intensities of the ionic complexes as a function of the FELIX frequency in the 230–560 cm^{-1} range using a time-of-flight mass spectrometer. From the recorded depletion spectra, IR absorption spectra are established as described previously.[55]

2.2 Theoretical methods

While density functional theory (DFT) methods are widely used in the determination of cluster structures and properties, no single functional consistently describes all their properties accurately. A specific type of clusters should be studied by using appropriate functionals. In previous studies on singly transition metal doped silicon clusters,[18,32,34,59] we found that the hybrid B3P86 functional in conjunction with the 6-311+G(d) basis set is able to well describe their geometric and electronic structures as well as to provide their vibrational spectra in good agreement with experiments. For the sake of facilitating a comparison with these previous studies, we again choose the B3P86 functional and the 6-311+G(d) basis set to investigate the geometries and vibrational spectra for the CrSi$_n$ series in the singly charged cationic and anionic as well as neutral states.

Because the energy differences between isomers are often small, a further comparison of relative energies is performed using the correlation consistent aug-cc-pVTZ basis set with the same B3P86 functional in some cases. Results presented in Table S1 of the ESI† show that most of the series of clusters considered hold the same energetic ordering of isomers at both levels of theory, except for the cationic CrSi$_6^+$, neutral CrSi$_7$, CrSi$_{10}$ and anionic CrSi$_7^-$ in which some small changes in the energetic ordering occur. Unless otherwise noted, the relative energy values quoted in the following sections are obtained at the B3P86/6-311+G(d)+ZPE level. Due to abundance of local minima on the potential energy surface of each cluster size, we include only the lowest-lying isomers whose relative energies are in proximity of the most stable isomer (with a relative energy of <1 eV).[60,61]

For the location of the cationic CrSi$_n^+$ and neutral CrSi$_n$ isomers, initial guess structures are generated by considering stable geometries of cationic, anionic, neutral metal and non-metal doped Si clusters reported in the literature.[3,9,31,32,34,39,40,59,62–69] Additionally, geometries of the pure Si clusters in different charge states taken from previous studies[31,34,37,42,44,70–73] are used as starting structures on which the Cr atom is added at various positions or an atom of the Si frame is replaced by a Cr atom. These structures are subsequently optimized in different multiplicities, from the singlet to the septet state for systems with an even number of electrons, and from the doublet to the octet state for systems with an odd number of electrons. In case that a geometry optimization converges in a new structure in a certain spin state, it is then taken for a new optimization cycle in other spin states. In case that similar structures have very small energy differences, they are re-optimized under symmetry constraints to verify the stable geometries.

Although a large number of initial structures are created, only a small number, being <15, of true energy minimum structures are attained for each size, confirming that both cationic CrSi$_n^+$ and neutral CrSi$_n$ clusters are only stable at some specific geometries (cf. the following section). Geometry optimizations are followed by calculations of harmonic vibrational frequencies to confirm the identity of the optimized stationary points. The latter are then used, without applying any scaling factor, to simulate their vibrational spectra by convoluting each harmonic mode with a Gaussian line shape with a full width at half maximum of 3 cm^{-1}. Harmonic vibrational frequencies are also used for evaluating the zero-point energies (ZPE) that are needed as corrections to relative energies between isomers based on the total energies. Although the ZPE corrections seem to be canceled out since ZPEs of isomers at the same size are roughly similar,[74] for the sake of completeness, they are included in the present evaluation.

For the identification of the two enantiomers of a chiral cluster's pair, the time-dependent density functional theory method (TD-DFT) at the B3P86/6-311+G(d) level is used to construct the corresponding electronic circular dichroism (CD) spectra. The **L**- and the **R**-notations are used for optical isomers with an up-direction and a down-direction spectrum, respectively. All the quantum chemical calculations are conducted by using the Gaussian 09 package.[75]

3. Results and discussion

Conventionally, the isomers discussed hereafter are denoted by **Xn-isoY** where X = **C** (cation), **N** (neutral) and **A** (anion), n = 3–10 identifies the number of Si atoms, and Y = 1, 2, 3... enumerates the isomers according to their increasing relative energy. Accordingly, **Xn-iso1** invariably refers to the lowest-lying isomer of the **Xn** series, and relative energies of other isomers are given with respect to its reference.

3.1 CrSi$_3^{+/0/-}$, CrSi$_4^{+/0/-}$ and CrSi$_5^{+/0/-}$

Fig. 1 and Fig. S2, S3, S14 (ESI† file) show structures, relative energies and electronic states of the low-lying cationic, neutral and anionic isomers for n = 3, 4 and 5. The most stable isomers of CrSi$_3^+$, CrSi$_3$ and CrSi$_3^-$ share a common planar rhombic shape with the Cr atom placed at an acute angle. Similarly, the lowest-lying isomer of CrSi$_4^+$ also has a planar structure with the Cr atom capping an edge of a rhombic Si$_4$ cluster. However, the lowest-lying neutral and anionic CrSi$_4^{0/-}$ isomers adopted a 3D distorted trigonal bipyramidal structure with the Cr atom situated at an equatorial position. At n = 5, all three charge states of the clusters adopt 3D shapes, and the lowest-lying structure of CrSi$_5^+$ has Cr placed at an axial position, while in both neutral and anionic states Cr is located at an equatorial position of the distorted octahedron.

3.2 CrSi$_6^{+/0/-}$

Cation. Fig. 2 depicts the structures of four lowest-lying isomers **C6-iso1**-**C6-iso4** (cf. Fig. S4 for higher energy structures, ESI†) of CrSi$_6^+$. All are formed upon addition of the Cr atom

15342 | *Phys. Chem. Chem. Phys.*, 2023, **25**, 15340–15353
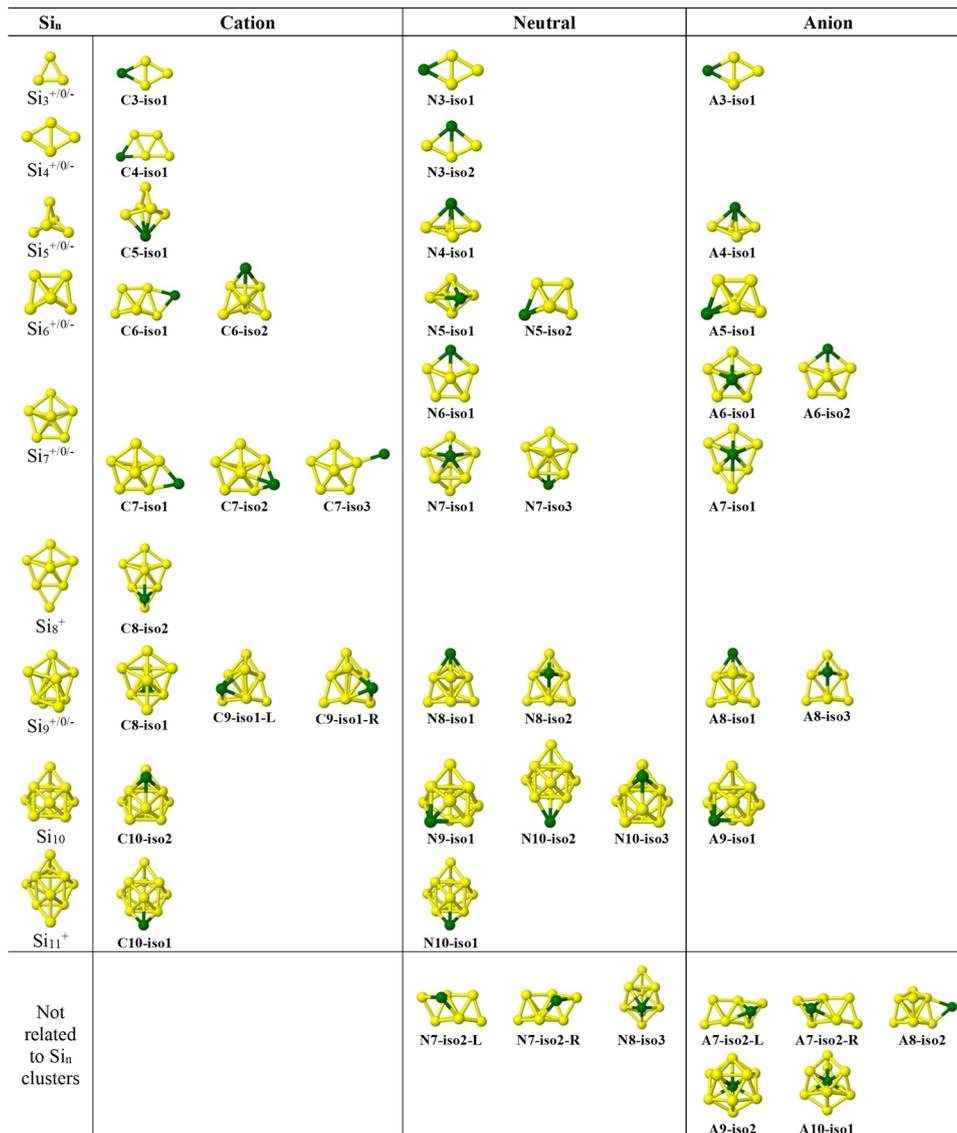
This journal is © the Owner Societies 2023

Fig. 1 Diagram illustrating the structural evolution of cationic, neutral and anionic chromium doped silicon clusters in comparison with the pure silicon clusters. Structures of cationic, neutral, anionic pure silicon clusters are taken from ref. 42–44, 67, 70–73 and re-calculated at the B3P86/6-311+G(d) level.

onto an edge or a face of the distorted octahedron Si_6. Their calculated IR spectra are compared to the experimental IR-MPD spectrum of the $CrSi_6^+ \cdot Ar$ complex. Although B3P86/6-311G(d) calculations predict the Cr-edge-capping **C6-iso1** (C_s, $^6A'$) as the lowest-lying isomer, its calculated IR spectrum shows some correspondence but does not fully agree with the experiment. In particular, the intense band located at $\sim$375–400 cm^{-1} and the lower-intensity band at $\sim$325–335 cm^{-1} do not appear in the computed spectrum. Besides, a calculated low-intensity peak at 525 cm^{-1} is not observed in the experimental spectrum.

On the other hand, the C_s **C6-iso2** ($^6A'$, +0.03 eV) shows a better agreement with the experimental IR-MPD spectrum (Fig. 2) because its calculated 383 cm^{-1} band corresponds to the experimental $\sim$375–400 cm^{-1} feature, and the combination of calculated signals at 433, 447 and 451 cm^{-1} also fits the

broad experimental band from $\sim$425 to $\sim$460 cm^{-1}. At the B3P86/aug-cc-pVTZ level, the **C6-iso2**-sextet isomer turns out to be 0.008 eV lower in energy than **C6-iso1**-sextet. In view of their tiny energy difference, these two isomers are basically degenerate and competitive for the global minimum isomer of the $CrSi_6^+$ cluster, in which **C6-iso2** appears to match better with the experimental IRMPD spectrum. The **C6-iso3** (+0.10 eV) and **C6-iso4** (+0.11 eV) isomers in the sextet state also are taken into account since they possess specific IR signals within the observed regions (the broad bands of $\sim$375–400 cm^{-1} and $\sim$425–460 cm^{-1}). However, their spectra insufficiently describe the experiment in the $\sim$200–350 cm^{-1} range and therefore are unlikely to contribute to the experimental spectrum.

Overall, of all the studied isomers of $CrSi_6^+$, the two degenerate and competitive isomers **C6-iso1** and **C6-iso2** in their
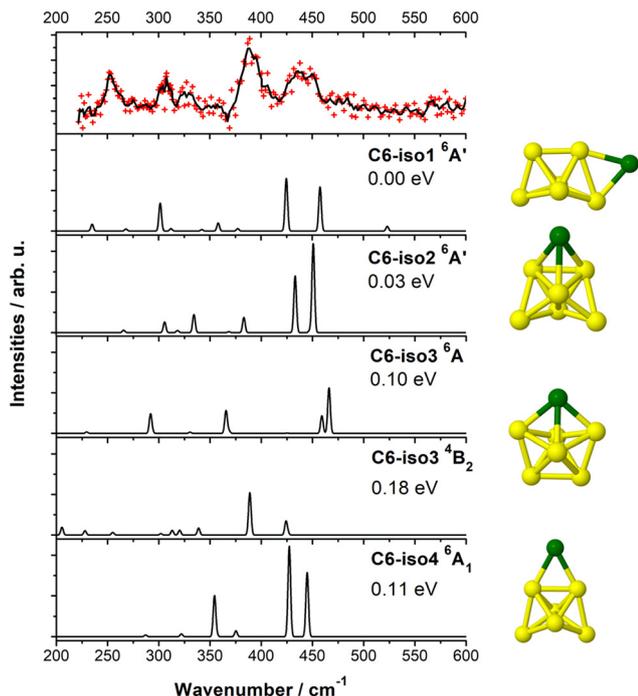
This journal is © the Owner Societies 2023

Phys. Chem. Chem. Phys., 2023, **25**, 15340–15353 | **15343**

Fig. 2 IR-MPD spectrum of $CrSi_6^+ \cdot Ar$ (upper panel) and simulated harmonic infrared spectra of low-energy isomers of $CrSi_6^+$ (B3P86/6-311+G(d)). Geometric structures of the low-energy isomers are shown on the right. Experimental data points are shown as red crosses, while the full black line corresponds to a three-point running average.

Fig. 3 IR-MPD spectrum of $CrSi_7^+ \cdot Ar$ (upper panel) and calculated harmonic infrared spectra (B3P86/6-311+G(d)) of low-energy isomers of $CrSi_7^+$.

sextet state give the best agreement to the experimental spectrum and may coexist in the experiment.

Anion and neutral. In an earlier work, the lowest-lying **A6-iso1** (C_{5v}, $^4A_1$) and the second lowest-lying **A6-iso2** (C_{2v}, $^6A_1$) isomers that have the Cr atom substituting an axial and an equatorial Si atom of the pentagonal bipyramid Si_7,[44] respectively, were assigned to contribute to the experimental photoelectron spectrum of the anionic $CrSi_6^-$ cluster with a larger contribution of the **A6-iso1**.[9] With B3P86/6311+G(d) calculations, the sextet **A6-iso2** isomer loses its C_{2v} symmetry as previously reported due to an imaginary frequency at $282i$ cm^{-1} of the latter.

The lowest-lying neutral $CrSi_6$ isomer is **N6-iso1** (C_{2v}, $^5B_2$), which has a shape similar to the anionic **A6-iso2** (*cf.* Fig. 1). Other neutral $n = 6$ isomers are at least 0.36 eV higher in energy with respect to **N6-iso1** (*cf.* Fig. S9, ESI†). Hence, no other structure effectively competes with **N6-iso1** for the ground-state of the neutral $CrSi_6$ cluster.

3.3 $CrSi_7^{+/0/-}$

Cation. Fig. 3 illustrates the three lowest-lying isomers **C7-iso1**, **C7-iso2** and **C7-iso3**. All are the most stable in a sextet spin state. They are formed by placing the Cr atom on an equatorial edge, a face and an equatorial apex of the Si_7 pentagonal bipyramid. Other isomers are much higher in energy and presented in Fig. S5 of the ESI.†
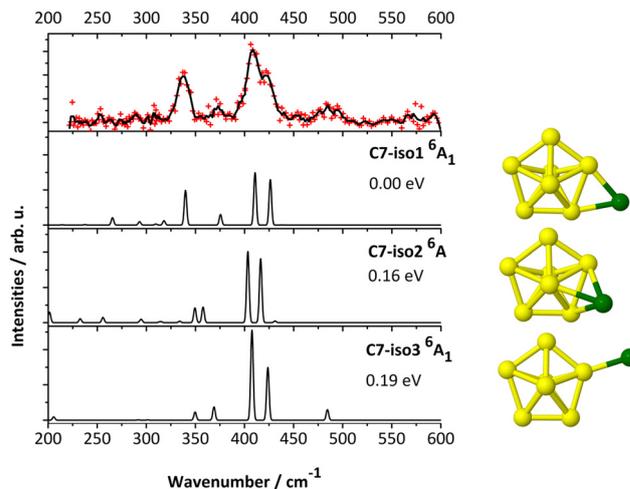
The simulated IR spectra of these three lowest-lying isomers share some similarities. The most striking common feature is the presence of two prominent peaks in the 390–430 cm^{-1} range, which correspond to normal vibrations of the Si_7 frame and fit very well with the intense bands centered at ~ 410 and ~ 425 cm^{-1} in the experimental spectrum. However, two other experimental features at ~ 340 and ~ 375 cm^{-1} only appear in the calculated spectrum of **C7-iso1**, while only the spectrum of **C7-iso3** displays a sign of the low-intensity experimental signal at ~ 485 cm^{-1}.

The infrared spectrum of the global minimum of $CrSi_7^+$, the Cr-edge-capped **C7-iso1** in a sextet state, matches very well with the experimental IR spectrum (Fig. 3). In view of their similar IR spectra, both **C7-iso2** and **C7-iso3** isomers, we cannot exclude that they contribute to the molecular beam with a smaller extent. We note that there may be unimolecular rearrangements between these isomers by the hopping of the Cr atom around the core Si cluster.

Anion and neutral. The lowest-lying **N7-iso1** (C_s) in a $^5A'$ state has a Cr atom located at an axial apex of the pentagonal bipyramid and an extra Si capped on a face of this frame (*cf.* Fig. 1). A pair of enantiomers **N7-iso2-L** and **N7-iso2-R** (+0.02 eV), and **N7-iso3** having Cr capped on a face of the pentagonal bipyramid Si_7 (+0.06 eV) are the second and third lowest-energy isomers (*cf.* Fig. S10, ESI†). At the B3P86/aug-cc-pVTZ + ZPE level, the energetic ordering is reversed with a marginal energetic preference of **N7-iso3**, whereas **N7-iso2-L/R** is now at +0.01 eV and **N7-iso1** at +0.05 eV (*cf.* Table S1, ESI†). These tiny energy differences suggest a real competition among the three isomers, and thus the **N7-iso1**, **N7-iso2-L/R**, **N7-iso3** could be regarded as degenerate ground state structures of the neutral $CrSi_7$ cluster.

Concerning the anions that have been analyzed before,[9] a pair of stable enantiomers at $n = 7$ is now discovered, including **A7-iso2-L** and **A7-iso2-R** whose structures are similar to the neutral pair **N7-iso2-R** and **N7-iso2-L**, respectively (*cf.* Fig. S10

and S14, ESI†). When recalculating their energies at the B3P86/aug-cc-pVTZ level, there is again a reversed energetic order in such a way that the pair of enantiomers **A7-iso2-L/R** has the lowest energy, marginally below **A7-iso1** in both quartet and sextet states (by only 0.04 eV). As in the neutral state, this anion basically is characterized by a degenerate ground state.

3.4 CrSi$_8^{+/0/-}$

Cation. The two lowest-lying isomers **C8-iso1** in the $^4A''$ state and **C8-iso2** in the $^6A'$ state (+0.06 eV) both possess C_s symmetries (cf. Fig. S6 and S15 for other isomers, ESI†). While the shape of **C8-iso1** is similar to that of the ground state of Si$_9^+$,[39] in which a Si atom capped onto a face of the pentagonal bipyramid is replaced by the Cr atom, **C8-iso2** is formed following addition of the Cr atom onto a Si$_8^+$ pattern.[39] The spectra of both isomers show certain similarities with the rich experimental spectrum of the CrSi$_8^+$·Ar complex, but the agreement is not entirely satisfactorily with either of them (cf. Fig. 4). Rather a combination of both calculated spectra can explain the experimental observation. In fact, both IR spectra have vibrational modes at 430 and 460 cm^{-1} corresponding to stretching modes of the silicon frame, and in agreement with the CrSi$_8^+$·Ar experimental broad band in the $\sim$420–470 cm^{-1} range. Also, the experimental features in the low-energy range at $\sim$240, $\sim$260 and $\sim$310 cm^{-1} have counterparts in both calculated spectra. There is a broad band of experimental absorption features from 360 to 470 cm^{-1}. In the calculated spectrum of **C8-iso2** a peak at 410 cm^{-1}, describing an asymmetric stretching vibration of the Si$_8^+$ cage, is much more intense than that in the experimental spectrum, but it might be related to the shoulder on the blue side of the intense 385 cm^{-1} feature. Similarly, the relative intensities of modes at $\sim$350 cm^{-1} in **C8-iso1** and $\sim$380 cm^{-1} in **C8-iso2** spectra are weaker than the highest intensity features centered at $\sim$350–360 and $\sim$380–400 cm^{-1} in the measured spectrum.

In summary, while the stable structure **C8-iso1** (C_s, $^4A''$) contributes to the experimental IR-MPD spectrum of the CrSi$_8^+$

cation, the presence of the higher spin isomer **C8-iso2** (C_s, $^6A'$) cannot be ruled out.

Anion and neutral. The most stable isomer of CrSi$_8$ **N8-iso1** (C_s, $^5A''$) has a structure similar to that of the anionic **A8-iso1**. The second lowest **N8-iso2** (C_s, $^5A''$, +0.05 eV) has a similar structure as the anionic **A8-iso3**. Both isomers are formed by substitution of a Si atom of the stable Si$_9$ frame (two extra Si atoms capping on two opposite faces of the pentagonal bipyramid)[44,73] by the Cr atom, in which Cr is placed at different apexes of the pentagonal bipyramid (cf. Fig. 1). The third isomer **N8-iso3** ($^3A'$, +0.06 eV) cannot be obtained by either addition or replacement of Cr in the stable Si frame (cf. Fig. S11, ESI†). These three isomers have an almost similar energy (difference of $\sim$0.01 eV at the B3P86/aug-cc-pVTZ level, cf. Table S1, ESI†). Hence, the **N8-iso1**, **N8-iso2** and **N8-iso3** isomers are likely to co-exist.

3.5 CrSi$_9^{+/0/-}$

Cation. The ten low-lying isomers of CrSi$_9^+$ are presented in Fig. S7 and S16 of the ESI.† Two pairs of enantiomers are found, of which one pair in the ^6A state **C9-iso1-L** and **C9-iso1-R** has the lowest relative energy. Their structures are formed by an addition of a Cr atom onto one of two faces that are symmetric to each other through a reflection plane of the most stable Si$_9$ frame.[44] This doping breaks the C_s symmetry of the Si$_9$ frame in such a way that the **C9-iso1-L** and **C9-iso1-R** chiral structures possess the same shape but cannot be superimposed. As expected, their calculated IR spectra are identical to each other, and they are in excellent agreement with the measured IR-MPD spectrum of CrSi$_9^+$·Ar (cf. Fig. 5). The intense peaks in the $\sim$440–480 cm^{-1} range correspond to stretching modes of the Si$_9$ frame, whose calculated frequencies at 450 and 475 cm^{-1} for **C9-iso1** match perfectly with experiment. Also the calculated frequencies at 426, 406, 385 and 368 cm^{-1} as well as ten normal modes in the 250–350 cm^{-1} range agree well with the experimental spectrum both in frequency and relative amplitudes. Spectra of other isomers do not fit the experimental CrSi$_9^+$·Ar spectrum well (cf. Fig. S16, ESI†). Hence, the enantiomeric pair
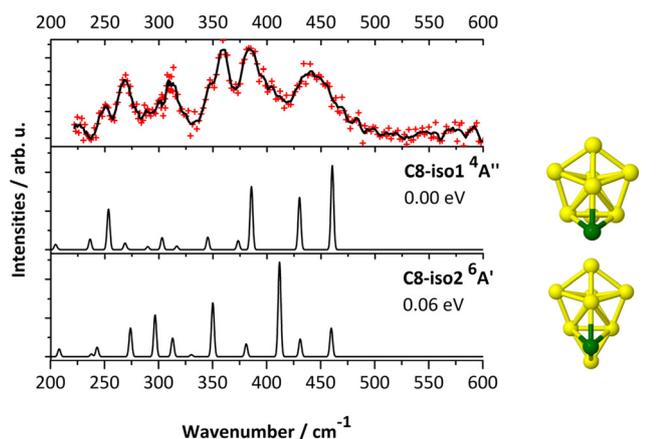

Fig. 4 IR-MPD spectrum of CrSi$_8^+$Ar (upper panel) and calculated harmonic infrared spectra (B3P86/6-311+G(d)) of low-energy isomers of CrSi$_8^+$.
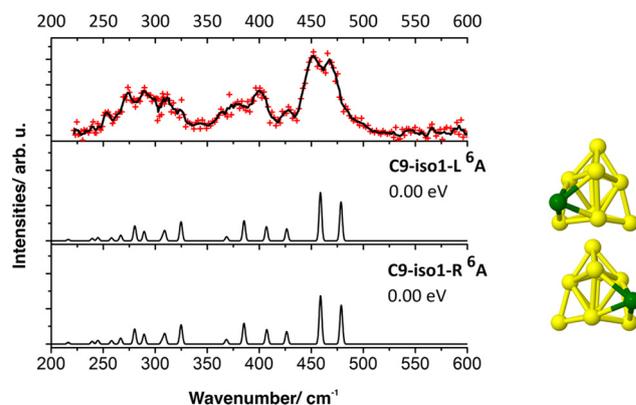

Fig. 5 IR-MPD spectrum of CrSi$_9^+$·Ar (upper panel) and calculated harmonic infrared spectra (B3P86/6-311+G(d)) of low-energy isomers of CrSi$_9^+$.

This journal is © the Owner Societies 2023

Phys. Chem. Chem. Phys., 2023, **25**, 15340–15353 | **15345**

of **C9-iso1-L** and **C9-iso1-R** isomers in the sextet state can be assigned to the cationic $CrSi_9^+$ cluster in view of a good match between their computational and observed spectra.

Anion and neutral. The lowest-energy isomer of neutral **N9-iso1** (^5A state) and anion **A9-iso1** (^6A state) have similar shapes arising from a displacement of a prismatic Si atom of the tetra-capped trigonal prism (TTP) frame by the Cr atom. The second lowest-energy isomers of the neutral are an enantiomeric pair, **N9-iso2-L** and **N9-iso2-R** (^5A, +0.07 eV). These chiral isomers have a distorted structure that does not follow any of previously known structures of Si clusters. The energetic order between **N9-iso1** and the pair **N9-iso2-L/R** remains unchanged but with a consistently small difference as they are re-calculated at the B3P86/aug-cc-pVTZ level (*cf.* Table S1, ESI†). According to that sequence, **N9-iso1** can be assigned as the lowest-lying energy structure of the neutral Si_9Cr cluster.

3.6 $CrSi_{10}^{+/0/-}$

Cation. Fig. 6 shows the experimental IR spectrum of $CrSi_{10}^+\cdot Ar$ and simulated vibrational spectra corresponding of seven low-lying isomers of $CrSi_{10}^+$; two of them are enantiomeric isomers. **C10-iso1** (C_1, ^6A), **C10-iso2** (C_s, $^6A'$, +0.04 eV), **C10-iso3-L** and **C10-iso3-R** (C_1, ^6A, +0.10 eV) and **C10-iso6**

Fig. 6 IR-MPD spectrum of $CrSi_{10}^+\cdot Ar$ (upper panel) and calculated harmonic infrared spectra (B3P86/6-311+G(d)) of low-energy isomers of $CrSi_{10}^+$.

(C_{2v}, $^6A_1$, +0.34 eV) are based on the TTP structure of Si_{10}^+ and Si_{10},[42,44] with the Cr added onto different faces. They exhibit similar vibrations as the Si_{10} core. Only the spectrum of **C10-iso6** differs because of its higher symmetry structure (C_{3v}).

The computed spectra of both **C10-iso1** and **C10-iso2** (+0.04 eV) agree best with the experimental data. The highest intensity experimental band, peaking at $\sim$420 cm^{-1} corresponds to the two modes centered at $\sim$422 and $\sim$432 cm^{-1} of **C10-iso1**, $\sim$410 and $\sim$429 cm^{-1} of **C10-iso2**, $\sim$411 and $\sim$433 cm^{-1} of **C10-iso3-L/R**, or with the degenerate peak at $\sim$425 cm^{-1} in **C10-iso6**. All isomers have vibrational modes that agree with the broad experimental band between $\sim$445 and $\sim$470 cm^{-1}. Only the **C10-iso1** and **C10-iso2** sufficiently reproduce the 225 to 400 cm^{-1} low-frequency range. In view of the small relative energy difference between **C10-iso1** and **C10-iso2** and their comparable spectra, it is reasonable to again assume a co-existence of both isomers in the molecular beam.

Anion and neutral. While the lowest-lying structure of the neutral $CrSi_{10}$ cluster (**N10-iso1**, C_s, $^5A'$ state) is similar to the lowest-lying one of its cation (**C10-iso1**, C_1, ^6A state), **N10-iso2** (C_s, $^5A'$) and **N10-iso3** (C_{2v}, $^7A_1$) have a similar shape as **C10-iso6** and **C10-iso2** isomers respectively (*cf.* Fig. 1 and Fig. S8 and S13, ESI†). Calculations at both levels of theory give inherently small differences of their energy, being within $\sim$0.02 eV. Hence, **N10-iso1**, **N10-iso2** and **N10-iso3** can again plausibly be considered as degenerate ground state structures of the neutral $CrSi_{10}$ cluster.

While the assigned cationic and neutral isomers follow an exohedral motif retaining the Si_{10} TTP pattern plus a capping Cr atom onto different faces, the anionic **A10-iso1** possesses now an endohedral structure in which the Cr dopant is fully encapsulated by a Si cage.[9]

To get more insight into the similarity of the structure of **C10-iso1** and **N10-iso1** isomers, their molecular orbitals (MOs) are analyzed. The electron configuration of **C10-iso1** can be described as: $[(1S)^2(1P)^6(1D_a)^2(1D_b)^4(1D_c)^4(2S)^2(1F_a)^4(2D_a)^4(1F_b)^6(2P)^6//(2D_b)^1(2D_c)^1(2D_c)^1(1F_c)^1(1F_c)^1]$ or $[(1S)^2(1P)^6(1D)^{10}(2S)^2(2P)^6(1F)^{12}(2D)^7]$ while that of **N10-iso1** as:
$[(1S)^2(1P_a)^2(1P_b)^4(1D_a)^2(1D_b)^8(2S)^2(1F_a)^2(2D_a)^2(2D_b)^2(1F_b)^4(2P_a)^4(1F_c)^4(2P_b)^2(2D_c)^2//(2D_c)^1(2D_d)^1(1F_d)^1(1F_d)^1]$ or $[(1S)^2(1P)^6(1D)^{10}(2S)^2(2P)^6(1F)^{12}(2D)^8]$ (*cf.* Fig. 7), indicating that an electron on a 2D shell of the neutral isomer is removed to form the cationic counterpart. $(2D_b)^1(2D_c)^1(2D_c)^1(1F_c)^1(1F_c)^1$ and $(2D_c)^1(2D_d)^1(1F_d)^1(1F_d)^1$ are singly occupied MOs of the cationic and neutral $CrSi_{10}$ cluster, respectively. The subscripts a, b, c and d denote for the lifting of the degeneracy of the high angular momentum states (1P, 1D, 2P, 2D and 1F) due to the cluster's non-spherical symmetry.

3.7 Wavenumber region for motions of Cr dopant

Given the higher mass of the Cr dopant, vibrational modes involving the motion of Cr are mainly located in the wavenumber region below 200 cm^{-1}. Vibrations in the wavenumber range from 200 to 600 cm^{-1} are mainly complex combinations of Si–Si vibrations. But the exact location of the Cr dopant atoms influences the nuclear movement of the Si_n frame as a
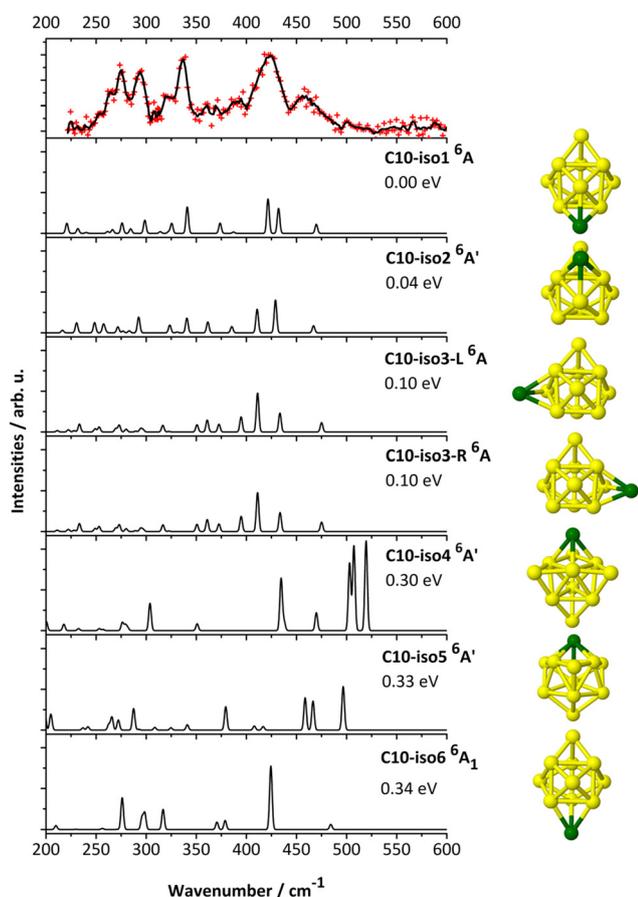
15346 | *Phys. Chem. Chem. Phys.*, 2023, **25**, 15340–15353
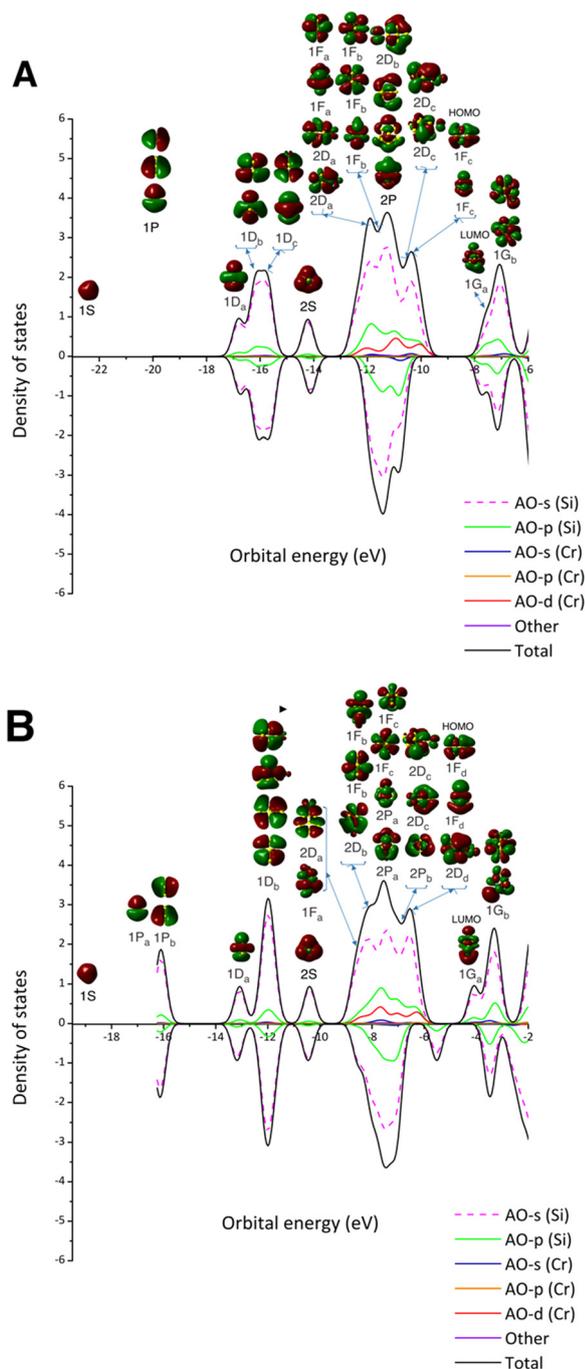
This journal is © the Owner Societies 2023

Fig. 7 Calculated density of states (DOS) of cationic CrSi$_{10}^+$ (A) and neutral CrSi$_{10}$ (B) and the projection of the DOS onto atomic orbitals (AO) of Si and Cr. Positive and negative DOS represent spin-up and spin-down electrons, respectively.

whole. Therefore the measured IR spectra are sensitive to the position of the dopant atom and the spectra of the chromium doped clusters as different from both the pure Si$_n^+$ (n = 6–10) cations[42] and Si$_n$ (n = 6, 7,10) neutral[43] clusters.

3.8 Growth mechanisms

Fig. 1 compares the structures of CrSi$_n^+$, CrSi$_n$ and CrSi$_n^-$ with each other and with the corresponding pure silicon clusters.

Overall, the most stable structures follow a consistent trend in which the Cr dopant is either adding onto, or replacing a Si atom in the stable pure silicon cluster with the same number of Si atoms. A few sizes do not follow this pattern, and they are presented at the bottom row of the figure.

All assigned cationic clusters whose IR spectra match well with experiment, prefer a Cr addition onto either an edge, a face or a vertex of the pure Si$_n^{0/+}$. In view of the expected small differences in the interaction energies arising from these additions, several quasi-energetic isomers emerge.

Different from the cations, the neutral and anionic counterparts tend to a characteristic substitution. At the sizes of n = 3–9, the Cr atom prefers to replace various Si positions of the Si$_{n+1}$ framework in both neutral and anionic states. However, at n = 10, while the neutral acts to retain the TTP frame, an exohedral-to-endohedral structural change occurs for the anion. The different growth mechanisms of the three charge states strengthens the viewpoint that the structural motif of a cluster is strongly impacted by, or even a manifest of, the total charge.

3.9 Relationship between charge effects, magnetisms and bonding

Natural electron configurations (NEC) and spin densities are evaluated by using the NBO 5.G program[76] at the B3P86/6-311+G(d) level. The average binding energies and fragmentation energies are calculated at the same level to probe the stability of clusters. The formulas employed are set forth as follows:

$$E_{\text{b-C}} = [nE(\text{Si}) + E(\text{Cr}^+) - E(\text{Si}_n\text{Cr}^+)]/(n+1) \quad (1)$$

$$E_{\text{b-N}} = [nE(\text{Si}) + E(\text{Cr}) - E(\text{Si}_n\text{Cr})]/(n+1) \quad (2)$$

$$E_{\text{b-A}} = [(n-1)E(\text{Si}) + E(\text{Si}^-) + E(\text{Cr}) - E(\text{Si}_n\text{Cr}^-)]/(n+1) \quad (3)$$

$$D_{\text{C}}(\text{Cr}^+) = E(\text{Si}_{n,\text{non-relaxed}}) + E(\text{Cr}^+) - E(\text{Si}_n\text{Cr}^+) \quad (4)$$

$$D_{\text{N}}(\text{Cr}^+) = E(\text{Si}_n^-{}_{,\text{non-relaxed}}) + E(\text{Cr}^+) - E(\text{Si}_n\text{Cr}) \quad (5)$$

$$D_{\text{N}}(\text{Cr}) = E(\text{Si}_{n,\text{non-relaxed}}) + E(\text{Cr}) - E(\text{Si}_n\text{Cr}) \quad (6)$$

$$D_{\text{A}}(\text{Cr}) = E(\text{Si}_n^-{}_{,\text{non-relaxed}}) + E(\text{Cr}) - E(\text{Si}_n\text{Cr}^-) \quad (7)$$

$$D_{\text{C/N/A}}(\text{Si}) = E(\text{Si}_{(n-1)}\text{Cr}^{+/0/-}) + E(\text{Si}) - E(\text{Si}_n\text{Cr}^{+/0/-}) \quad (8)$$

Eqn (1)–(3) define the average binding energies of cationic, neutral and anionic Cr-doped silicon clusters, respectively. Eqn (4)–(7) provide the dissociation energies of removing either a Cr atom or a Cr$^+$ ion from the cationic, neutral and anionic Cr doped silicon clusters. Finally, eqn (8) gives the dissociation energy for removal of a Si atom.

The Wigner–Witmer spin conservation rule is applied to calculate both the average binding energy and fragmentation energy as it was suggested to give reasonable results in the case of CrSi$_{14}$.[77] The removed Si atoms have similar positions in the corresponding structures of the cationic, neutral and anionic clusters considered. The Cr$^+$ cation and Cr atom are removed from the cationic and anionic isomers, respectively. In case of the neutral clusters, both removal of the Cr$^+$ cation and the Cr atom are considered.

This journal is © the Owner Societies 2023

Phys. Chem. Chem. Phys., 2023, **25**, 15340–15353 | **15347**

Table 1 Average binding energy, fragmentation energies and natural population analysis for the lowest-lying isomers of the cationic, neutral, anionic $CrSi_n^{+/0-}$ clusters (B3P86/6-311 + G(d))

Isomer		State	$D_{C/N}$ (Cr$^+$)	$D_{N/A}$ (Cr)	$D_{C/N/A}$ (Si)	$E_{b-C/N/A}$	Atomic charge on Cr	Electron population on Cr's 3d shell	Electron population on Cr's 4s shell	Spin density of Cr	Total Wiberg bond of Cr	Total Wiberg bond of cleaved Si
Cation	C3-iso1	$^4B_2$	4.77		5.02	2.40	0.83	4.86	0.30	4.54	1.36	2.32
	C4-iso1	$^6A'$	2.10		5.70	2.74	0.84	4.92	0.23	4.82	0.66	2.23
	C5-iso1	$^6A'$	2.58		5.98	2.95	0.77	4.90	0.29	4.62	1.04	2.79
	C6-iso2	$^6A'$	2.19		6.55	3.11	0.82	4.94	0.21	4.73	0.74	2.41
	C7-iso1	$^6A_1$	2.32		6.20	3.27	0.83	4.96	0.20	4.87	0.55	2.83
	C8-iso1	$^4A''$	5.20		5.72	3.23	0.78	4.97	0.22	4.34	1.45	2.48
	C9-iso1-L/R	^6A	2.42		6.33	3.33	0.75	5.03	0.18	4.54	0.91	2.76
	C10-iso1	^6A	2.52		7.07	3.42	0.82	4.96	0.20	4.71	0.74	2.98
Neutral	N3-iso1	$^5A_1$	6.78	3.69	4.96	2.59	0.66	4.94	0.38	4.67	1.22	2.74
	N4-iso1	$^5B_2$	6.76	2.87	5.62	2.89	0.61	4.98	0.33	4.56	1.32	2.65
	N5-iso1	$^5B_1$	7.27	4.22	6.07	3.12	0.58	4.99	0.36	4.47	1.50	2.85
	N6-iso1	$^5B_2$	6.77	3.25	5.92	3.25	0.64	5.05	0.25	4.44	1.34	2.79
	N7-iso1	$^5A'$	7.44	4.14	5.67	3.26	0.44	5.04	0.40	4.32	1.76	2.63
	N8-iso1	$^5A''$	6.40	3.85	5.67	3.30	0.58	5.14	0.22	4.31	1.38	2.73
	N9-iso1	^5A	6.82	4.15	6.40	3.36	0.56	5.10	0.23	4.18	1.60	3.02
	N10-iso1	$^5A'$	6.14	2.80	6.09	3.43	0.67	5.04	0.27	4.59	1.02	2.68
Anion	A3-iso1	$^6A_1$		3.06	5.69	2.80	0.30	4.99	0.66	5.08	1.04	2.96
	A4-iso1	$^4A_2$		5.34	6.15	3.00	0.42	5.09	0.40	4.38	1.81	2.78
	A5-iso1	$^6A'$		3.37	7.07	3.29	0.46	5.05	0.44	4.87	1.03	2.84
	A6-iso1	$^4A_1$		7.42	7.29	3.37	0.24	5.04	0.57	4.15	2.41	3.07
	A7-iso1	$^6A'$		4.40	6.39	3.38	0.28	5.14	0.41	4.51	1.48	3.06
	A8-iso1	$^6A_1$		3.24	6.33	3.45	0.52	5.21	0.23	4.54	1.03	2.98
	A9-iso2	^6A		3.75	6.19	3.50	0.43	5.23	0.23	4.43	1.21	3.06
	A10-iso1	^2A		10.73	6.33	3.55	-2.64	7.77	0.45	0.81	4.22	2.91

Energetic stability. There appears to be an inverse relationship between the multiplicity and the total Wiberg bond index as well as with the Cr fragmentation energy (*cf.* Table 1 and Table S4, ESI†). The total Wiberg bond indices and dissociation energies follow a similar size dependency (*cf.* Fig. 8A and B), demonstrating a strong correlation between the Cr coordination number and the stability of the Si–Cr bonds. The Si–Cr dissociation energies are also related to the spin multiplicities of the clusters, *i.e.* the lower the multiplicity is, the larger the Cr fragmentation energy. This is easily recognized with C8-iso1, N8-iso3, N10-iso2, A6-iso1 and especially in A7-iso1. At a lower multiplicity of the cluster, the Cr atom receives more electrons from Si (larger value of electron population on Cr (*cf.* Table S3, ESI†), and thus stronger Si–Cr bonds are created rendering the Cr fragmentation more difficult.

The Si–Si bond dissociation energy depends mainly on the charge and structure of the cluster. Overall, for the small sizes $n = 3-5$ the trends for the dissociation of a Si atom are similar in the cationic, anionic and neutral species (*cf.* Fig. 9A). These small-sized clusters have low binding energies per atom. In the $n = 6-8$ size range, either neutral or anionic, the Si–Si dissociation energy is related to the strong binding of the pentagonal bipyramidal frame. Removal of a Si atom located at a vertex of the pentagonal bipyramid turns out to be more difficult than a Si atom capped onto a face or an edge-doped position. Properties of a pair of neutral and anionic clusters become totally different from each other at the size of $n = 10$, due to the large structural difference between the exohedral (neutral) and the endohedral (anion) cluster.

In the case of cationic clusters, there are two opposite tendencies in the $D_C(Cr^+)$ and the $D_C(Si)$ curves (*cf.* Fig. 8A and 9A), demonstrating that if the Si–Si bond is getting stronger, it is easier to remove a Cr atom from the Si cluster.

In summary, while the Cr and Cr$^+$ dissociation energies are impacted by the total Wiberg bond index and the multiplicity, the strength of Si–Si bonds is more affected by the cluster's charge and structure. A cluster becomes thermodynamically more stable when its size increases. Generally, the average binding energies of cationic, neutral and anionic clusters become larger from $n = 3$ to $n = 10$ except for C8-iso1, C8-iso2 (Fig. 10A and Table S3, ESI†), showing that the cationic CrSi$_8^+$ is slightly less stable.

In Fig. 10A, the ordering $E_{b-A} > E_{b-N} > E_{b-C}$ demonstrates the important role of the charge state on the stability. Moreover, the adiabatic ionization energies (IE$_a$) and the adiabatic electron affinities (EA$_a$) of the lowest-lying neutral isomers in Table 2 (*cf.* Table S4 for other structures, ESI†) are also significantly size-dependent. While the IE$_a$ values amount to 7–8 eV, the EA$_a$ are relatively large, being in the range of 2.5 to 3.3 eV, indicating the high stability of the anions.

Charge effects, magnetism and the polar covalent bond. On the basis of bond lengths and electron charge density values, it was suggested that at small sizes, the CrSi$_n$ prefers a "tight bonding" with an exohedral structure.[12] From $n = 12$, the endohedral motif becomes more favorable, and the covalent bond is more preferred for Si–Cr.[12] In all the clusters with $n = 3-10$ considered in this study, the local charge on the Cr center is about halfway between 0 and 1. Such a polarization of Si–Cr bonds belonging to exohedral clusters is reinforced when the net charges on Cr are positive, while the charges on Si atoms directly bound to Cr are predominantly negative. This observation lends further support for the conjecture that the Si–Cr
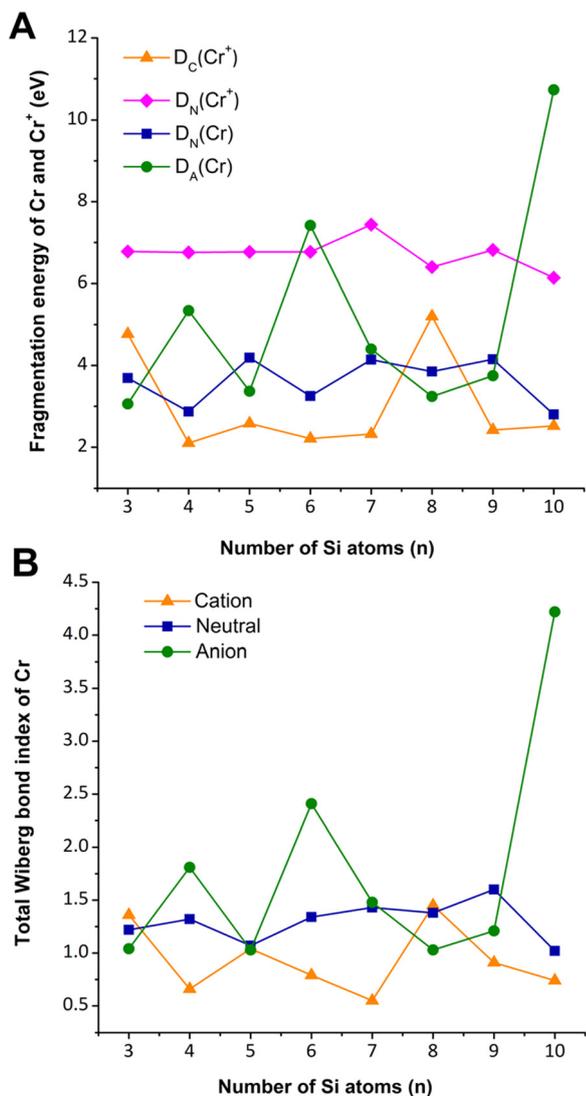
Fig. 8 Fragmentation energy to remove either Cr or Cr$^+$ (A) and total Wiberg bond index of Cr (B), in the lowest-energy cationic, neutral and anionic lowest-lying CrSi$_n^{+/0/-}$ isomers with n = 3–10. Calculated values are obtained from B3P86/6-311+G(d) + ZPE computations.
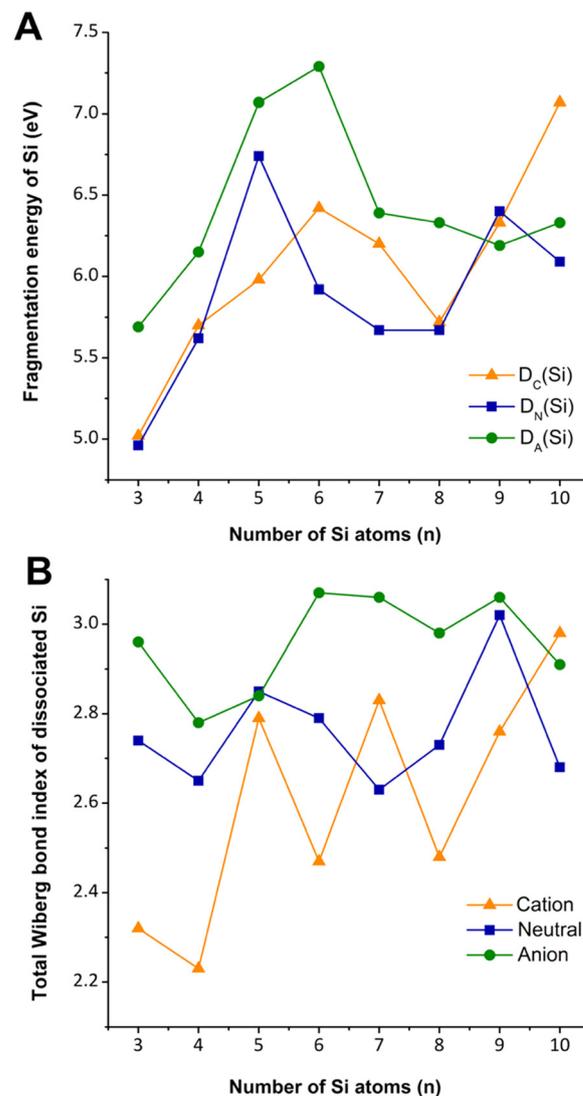

Fig. 9 Fragmentation energy to remove a Si atom (A) and total Wiberg bond index of dissociated Si (B), in the lowest-energy cationic, neutral and anionic lowest-lying CrSi$_n^{+/0/-}$ isomers with n = 3–10. Calculated values are obtained from B3P86/6-311+G(d) + ZPE computations.

bonds are polar covalent bonds whose positive δ^+ poles are located on the Cr center and negative δ^- poles on the Si one, except for **A9-iso2** and **A10-iso1** that have endohedral structures. As these Si–Cr bonds are more delocalized, they allow for a flexible movement of the Cr atom on the Si frames giving rise to quasi-degenerate isomers.

The spin densities on the Si atoms turn out to be very small or even insignificant ($\sim$ 0.0–0.3 e) in comparison to that of Cr, indicating that electrons on Si centers are actually paired. The number of electrons on the atomic orbital (AO) of AO-3s(Si) decrease by $\sim$0.3–0.5 e whereas they increase in AO-3p(Si) by $\sim$0.3–0.7 e, indicating the typical hybridization between the 3s and 3p orbitals of Si atoms.[10]

In terms of magnetic moments, charge distribution calculations (*cf.* Table 1) show that the index of electron occupation on Cr(3d) shells of the cationic cluster amounts

to $\sim$5 e, illustrating an occupancy of five single electrons on the 3d-AOs, while the electron density on the Cr (4s) shells are equal to only $\sim$0.2 e, showing the near absence of electrons in the 4s orbitals. Such an electron configuration, combined with the local spin densities on Cr ($\sim$ 4.5–5.0), elucidates why these CrSi$_n^+$ cations are more stable in the sextet state and it confirms that the magnetic moments are mainly located on Cr. The magnetic moments are equally concentrated mainly on the Cr atom for exohedral structures of neutral and anionic isomers as well (the local spin densities on the Cr atom being $\sim$4.2–4.6 for neutral isomers with sizes n = 3–10 and $\sim$4.2–5.1 for anionic isomers with sizes n = 3–9), highlighting the high magnetic moments majorly located on Cr counterparts, except for the endohedral **A9-iso2** and **A10-iso2** whose local spin densities on Cr are approximately equal to 1.
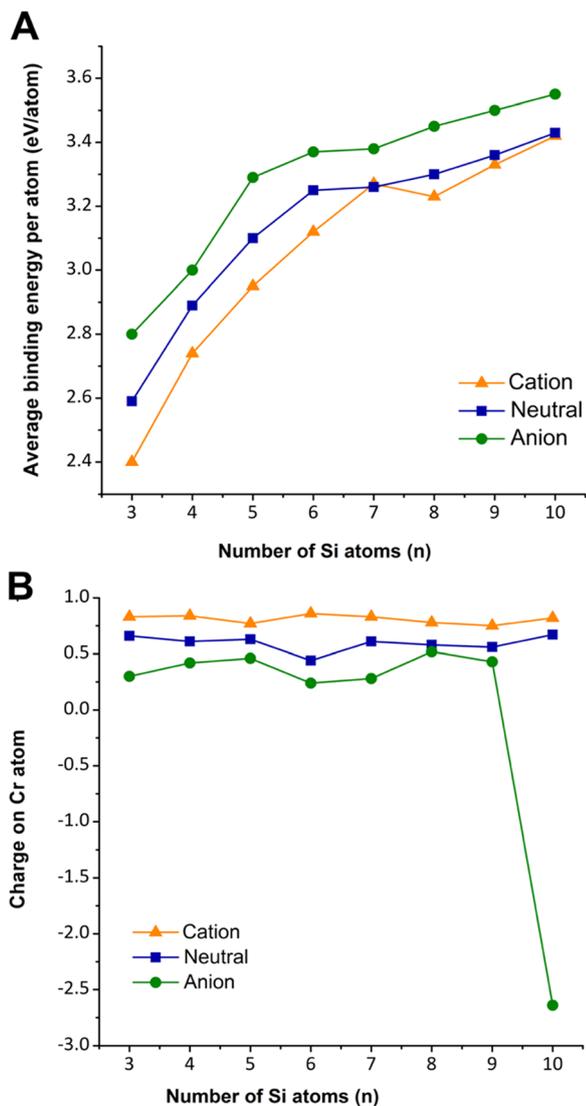
Fig. 10 Average binding energy per atom (A) and charges on Cr atom (B), in the lowest-energy cationic, neutral and anionic lowest-lying $CrSi_n^{+/0/-}$ isomers with $n = 3–10$. Calculated values are obtained from B3P86/6-311+G(d) + ZPE computations.

Table 2 Adiabatic ionization energies (IE_a) and adiabatic electron affinities (AE_a) of the lowest-lying neutral isomers (B3P86-6-311+G(d) + ZPE)

Neutral structure	IE_a (eV)	AE_a (eV)
N3-iso1	8.15	2.80
N4-iso1	7.23	2.54
N5-iso1	7.41	3.10
N6-iso1	7.50	2.52
N7-iso1	7.52	2.79
N8-iso1	7.41	3.28
N9-iso1	7.87	3.31
N10-iso1	6.62	3.05

The net atomic charges of Cr (0.7–0.8 e for cations, 0.4–0.6 e for neutral, 0.2–0.5 e for anions excepted **A10-iso1**) (*cf.* Table 1) show that the total charges are not completely localized on Cr atoms but rather dispersed over the cluster.
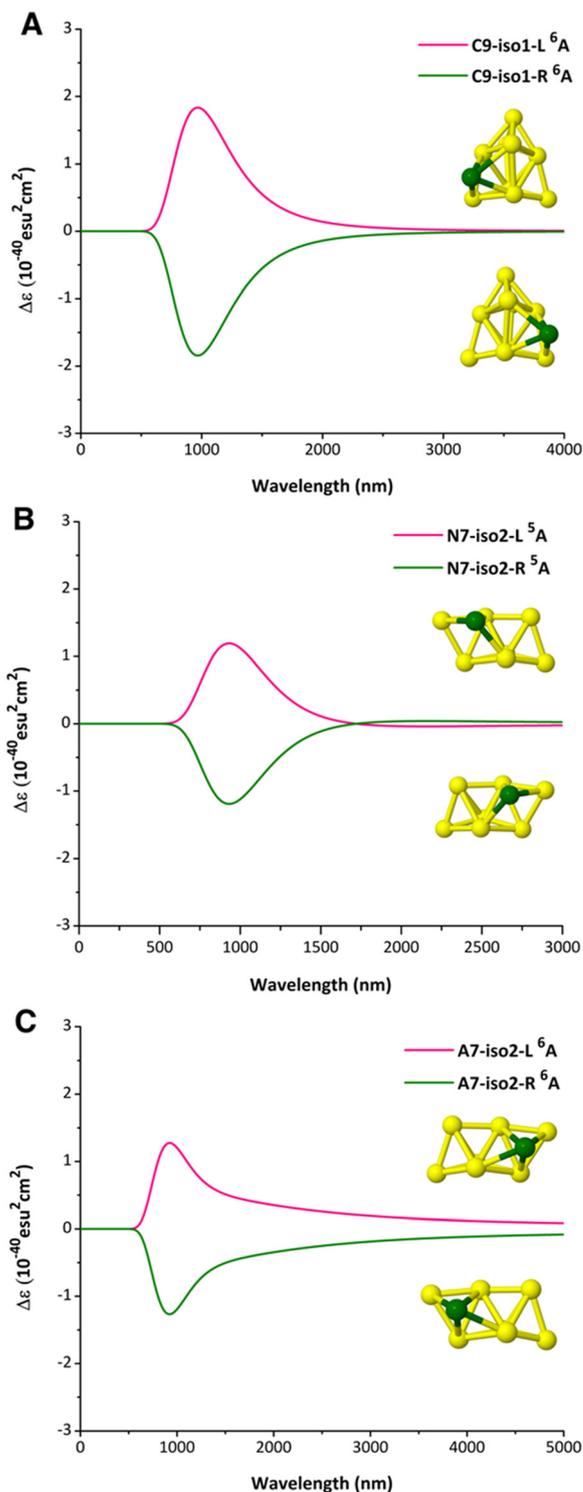

Fig. 11 Electronic circular dichroism (ECD) spectra of the lowest-lying energy enantiomers (A): $CrSi_9^+$, (B): $CrSi_7$ and (C): $CrSi_7^-$ calculated by the TD-B3P86/6-311+G(d) method.

3.10 Chirality

It has been established that a molecule may be chiral, and thereby optically active, only if it does not possess an improper rotation axis.[78] There are four different types of chirality in

15350 | *Phys. Chem. Chem. Phys.*, 2023, **25**, 15340–15353

This journal is © the Owner Societies 2023

inorganic nanostructures,[79] namely, (1) asymmetry of the inorganic core of the nanoparticles, (2) chirality of the inorganic surface, (3) chirality of the stabilizer shell, and (4) chirality by a chiral field effect. It appears that in the series considered here, the Cr-doping leads to chiral enantiomers that exhibit an intrinsic chirality of the cluster core, and can thus be assigned as a first type inorganic nanoscale chirality. Exohedral geometries combined with bond length difference between Si–Cr and Si–Si often lead to a symmetry breaking.

A cluster at different multiplicity may have different geometric symmetries. In some cases, its structure is lowered to a C_1 point group inducing chiral structures. For example, in the case of the pair of **C8-iso5-L** and **C8-iso5-R** isomers, they are stable enantiomers of each other at the sextet state, but they converge to the same structure at the quartet state bearing a C_s point group (*cf.* Fig. S6, ESI†).

As presented above, we discover in the present study three ground state enantiomeric pairs corresponding to the cationic $CrSi_9^+$ (**C9-iso1-L/R**), the neutral $CrSi_7$ (**N7-iso2-L/R**) and the anionic $CrSi_7^-$ (**A7-iso2-L/R**) (*cf.* Fig. 11). These exohedral enantiomers can be built up by interlocking the trigonal bipyramidal blocks together and the Cr atom is located at an equatorial vertex of one of these interlocking trigonal bipyramidal blocks.

Evidently, the two clusters of an enantiomeric pair share with each other an identical IR spectrum as well as undistinguishable UV-Vis spectra (*cf.* Fig. S17, ESI†). In order to distinguish them, the electronic circular dichroism (ECD) spectra are calculated by using the TD-DFT method at the B3P86/6-311+G(d) level. The ECD spectra of three ground state enantiomers are presented in Fig. 11, while the ECDs of the other pairs are presented in Fig. S18 (ESI†). As these exohedral enantiomeric structures exhibit both typical optical and magnetic properties, they can be regarded as possible building blocks for opto-magnetic nanomaterials.

4. Concluding remarks

The present combined experimental and theoretical study has led to a number of conclusions:

i. First, the exohedral structures with large magnetic moments of the cationic chromium-doped silicon clusters $CrSi_n^+$ with n = 6–10 have successfully been assigned by combining the IR-MPD spectra of the $CrSi_n^+ \cdot Ar$ complexes in the 200 to 600 cm^{-1} range with DFT calculations using the hybrid B3P86 functional and the 6-311+G(d) basis set.

ii. Second, an extensive structural comparison of the cationic, neutral and anionic clusters shows that the total charge significantly affects their structural evolution. While the Cr atom prefers an addition onto a pure silicon cluster in case of cations $CrSi_n^+$ (n = 3–10), the metal dopant favors a substitution in the neutral Si_nCr and anionic Si_nCr^- counterparts, except for the $CrSi_{10}^-$ anion which adopts an endohedral structure.

iii. Third, the large magnetic moments of the exohedral clusters (the local spin density of cationic, neutral and anionic

clusters is 4.2–5.0) are majorly located on Cr, indicating the highly intrinsic magnetic moment of the metallic atom is well conserved following doping, *i.e.* a sextet electronic state for cationic and anionic isomers and a quintet electronic state for neutral isomers. The Si–Cr bonds of $CrSi_n^{+/0/-}$ clusters in three charge states with n = 3–10 are polar covalent bonds. Apart from the endohedral anionic **A9-iso2** and **A10-iso1** clusters that have a negative charge on the Cr atom, the other considered clusters have exohedral structures with a positive charge centered on the Cr position.

iv. Last but not least, three pairs of lowest-lying energy enantiomers **C9-iso1-L/R**, **N7-iso2-L/R** and **A7-iso2-L/R** whose structures are interlocking the trigonal bipyramidal blocks, are discovered. These stable enantiomers inherently possessing both typical optical and magnetic properties are assigned as intrinsically chiral nanomaterials.

Conflicts of interest

The authors declare no competing financial interest.

Acknowledgements

References

1 S. M. Bhagyaraj, O. S. Oluwafemi, N. Kalarikkal and S. Thomas, *Synthesis of inorganic nanomaterials: advances and key technologies*, Woodhead Publishing, Duxford England, Cambridge, MA, 2018.

2 M. T. Nguyen and B. Kiran, *Clusters: Structure, Bonding and Reactivity*, Springer International Publishing, Cham, 1st edn, 2017.

3 P. Claes, E. Janssens, V. T. Ngan, P. Gruene, J. T. Lyon, D. J. Harding, A. Fielicke, M. T. Nguyen and P. Lievens, *Phys. Rev. Lett.*, 2011, **107**, 173401.

4 S. Neukermans, X. Wang, N. Veldeman, E. Janssens, R. E. Silverans and P. Lievens, *Int. J. Mass Spectrom.*, 2006, **252**, 145–150.

5 R. K. Waits, *Thin Solid Films*, 1973, **16**, 237–247.

6 R. K. Waits, *Proc. IEEE*, 1971, **59**, 1425–1429.

7 D. Caputo, G. de Cesare, A. Nascetti and M. Tucci, *Thin Solid Films*, 2007, **515**, 7517–7521.

This journal is © the Owner Societies 2023

Phys. Chem. Chem. Phys., 2023, **25**, 15340–15353 | **15351**

8 M. Jhabvala, S. Babu, C. Monroy, M. M. Freund and C. D. Dowell, *Cryogenics*, 2002, **42**, 517–526.

9 X.-Y. Kong, H.-G. Xu and W. Zheng, *J. Chem. Phys.*, 2012, **137**, 064307.

10 B. Yang, H. Xu, X. Xu and W. Zheng, *J. Phys. Chem. A*, 2018, **122**, 9886–9893.

11 K. Wang, H.-Y. Zhao, L. Miao, Z.-Z. Jia, G.-J. Yin, X.-D. Zhu, R. Moro, B. von Issendorff and L. Ma, *J. Phys. Chem. A*, 2022, **126**, 1329–1335.

12 H. Kawamura, V. Kumar and Y. Kawazoe, *Phys. Rev. B: Condens. Matter Mater. Phys.*, 2004, **70**, 245433.

13 L.-j Guo, G.-f Zhao, Y.-z Gu, X. Liu and Z. Zeng, *Phys. Rev. B: Condens. Matter Mater. Phys.*, 2008, **77**, 195417.

14 S. N. Khanna, B. K. Rao and P. Jena, *Phys. Rev. Lett.*, 2002, **89**, 016803.

15 U. Farooq, S. Naz, H.-G. Xu, B. Yang, X. Xu and W.-J. Zheng, *Coord. Chem. Rev.*, 2020, **403**, 213095.

16 W. Zheng, J. M. Nilles, D. Radisic and K. H. Bowen Jr., *J. Chem. Phys.*, 2005, **122**, 071101.

17 M. B. Abreu, A. C. Reber and S. N. Khanna, *J. Phys. Chem. Lett.*, 2014, **5**, 3492–3496.

18 N. D. Phi, N. T. Trung, E. Janssens and V. T. Ngan, *Chem. Phys. Lett.*, 2016, **643**, 103–108.

19 J. Ulises Reveles and S. N. Khanna, *Phys. Rev. B: Condens. Matter Mater. Phys.*, 2005, **72**, 165413.

20 S. M. Beck, *J. Chem. Phys.*, 1987, **87**, 4233–4234.

21 S. M. Beck, *J. Chem. Phys.*, 1989, **90**, 6306–6312.

22 S. Neukermans, X. Wang, N. Veldeman, E. Janssens, R. E. Silverans and P. Lievens, *Int. J. Mass Spectrom.*, 2006, **252**, 145–150.

23 J. B. Jaeger, T. D. Jaeger and M. A. Duncan, *J. Phys. Chem. A*, 2006, **110**, 9310–9314.

24 J. T. Lau, K. Hirsch, P. Klar, A. Langenberg, F. Lofink, R. Richter, J. Rittmann, M. Vogel, V. Zamudio-Bayer, T. Möller and B. V. Issendorff, *Phys. Rev. A*, 2009, **79**, 053201.

25 D. Palagin, M. Gramzow and K. Reuter, *J. Chem. Phys.*, 2011, **134**, 244705.

26 E. Janssens, P. Gruene, G. Meijer, L. Wöste, P. Lievens and A. Fielicke, *Phys. Rev. Lett.*, 2007, **99**, 063401.

27 P. V. Nhat, N. T. Si, V. G. Kiselev, A. Fielicke, H. T. Pham and M. T. Nguyen, *Chem. Commun.*, 2022, **58**, 5785–5788.

28 P. Ferrari, G.-L. Hou, O. V. Lushchikova, F. Calvo, J. M. Bakker and E. Janssens, *Phys. Chem. Chem. Phys.*, 2020, **22**, 11572–11577.

29 P. V. Nhat, N. T. Si, N. T. N. Hang and M. T. Nguyen, *Phys. Chem. Chem. Phys.*, 2022, **24**, 42–47.

30 P. Ferrari, H. T. Pham, J. Vanbuel, M. T. Nguyen, A. Fielicke and E. Janssens, *Chem. Commun.*, 2021, **57**, 9518–9521.

31 V. T. Ngan, P. Gruene, P. Claes, E. Janssens, A. Fielicke, M. T. Nguyen and P. Lievens, *J. Am. Chem. Soc.*, 2010, **132**, 15589–15602.

32 Y. Li, N. M. Tam, A. P. Woodham, J. T. Lyon, Z. Li, P. Lievens, A. Fielicke, M. T. Nguyen and E. Janssens, *J. Phys. Chem. C*, 2016, **120**, 19454–19460.

33 X. Li, P. Claes, M. Haertelt, P. Lievens, E. Janssens and A. Fielicke, *Phys. Chem. Chem. Phys.*, 2016, **18**, 6291–6300.

34 V. T. Ngan, E. Janssens, P. Claes, J. T. Lyon, A. Fielicke, M. T. Nguyen and P. Lievens, *Chem. – Eur. J.*, 2012, **18**, 15788–15793.

35 V. T. Ngan, M. Haertelt, J. Lyon, A. Fielicke, M. T. Nguyen, P. Lievens and E. Janssens, *J. Chem. Phys.*, 2013, **138**, 194301.

36 Y. Li, J. T. Lyon, A. P. Woodham, P. Lievens, A. Fielicke and E. Janssens, *J. Phys. Chem. C*, 2015, **119**, 10896–10903.

37 P. Gruene, A. Fielicke, G. Meijer, E. Janssens, V. T. Ngan, M. T. Nguyen and P. Lievens, *Chem. Phys. Chem.*, 2008, **9**, 703–706.

38 V. Khanna, R. Singh, P. Claes, M. T. Nguyen, A. Fielicke, E. Janssens, P. Lievens and J. E. McGrady, *J. Phys. Chem. A*, 2022, **126**, 1617–1626.

39 J. Zhao, Q. Du, S. Zhou and V. Kumar, *Chem. Rev.*, 2020, **120**, 9021–9163.

40 Y. Li, J. T. Lyon, A. P. Woodham, A. Fielicke and E. Janssens, *Chem. Phys. Chem.*, 2014, **15**, 328–336.

41 Y. Li, *Geometric, Electronic and Magnetic Properties of Transition Metal Doped Silicon Clusters, and Development of a Magnetic Deflection Setup*, PhD thesis, KU Leuven, 2016.

42 J. T. Lyon, P. Gruene, A. Fielicke, G. Meijer, E. Janssens, P. Claes and P. Lievens, *J. Am. Chem. Soc.*, 2009, **131**, 1115–1121.

43 A. Fielicke, J. T. Lyon, M. Haertelt, G. Meijer, P. Claes, J. de Haeck and P. Lievens, *J. Chem. Phys.*, 2009, **131**, 171105.

44 M. Haertelt, J. T. Lyon, P. Claes, J. de Haeck, P. Lievens and A. Fielicke, *J. Chem. Phys.*, 2012, **136**, 064301.

45 K. R. Krishnadas, L. Sementa, M. Medves, A. Fortunelli, M. Stener, A. Fürstenberg, G. Longhi and T. Bürgi, *ACS Nano*, 2020, **14**, 9687–9700.

46 Q.-Y. Zhang and L. Zhao, *Tetrahedron Lett.*, 2018, **59**, 310–316.

47 Y. Wang, B. Nieto-Ortega and T. Bürgi, *Nat. Commun.*, 2020, **11**, 4562.

48 D. Zerrouki, J. Baudry, D. Pine, P. Chaikin and J. Bibette, *Nature*, 2008, **455**, 380–382.

49 Y. Sato, M. Mitani and H. Yao, *Phys. Chem. Chem. Phys.*, 2019, **21**, 14984–14991.

50 A. Lechtken, D. Schooss, J. R. Stairs, M. N. Blom, F. Furche, N. Morgner, O. Kostko, B. von Issendorff and M. M. Kappes, *Angew. Chem., Int. Ed.*, 2007, **46**, 2944–2948.

51 X. Gao, B. Han, X. Yang and Z. Tang, *J. Am. Chem. Soc.*, 2019, **141**, 13700–13707.

52 G. Deng, B. K. Teo and N. Zheng, *J. Am. Chem. Soc.*, 2021, **143**, 10214–10220.

53 J. Kumar, K. G. Thomas and L. M. Liz-Marzán, *Chem. Commun.*, 2016, **52**, 12555–12569.

54 Y. Li, T. Higaki, X. Du and R. Jin, *Adv. Mater.*, 2020, **32**, 1905488.

55 A. Fielicke, G. von Helden and G. Meijer, *Eur. Phys. J. D*, 2005, **34**, 83–88.

56 D. Oepts, A. F. G. van der Meer and P. W. van Amersfoort, *Infrared Phys. Technol.*, 1995, **36**, 297–308.

57 R. Ferrando, J. Jellinek and R. L. Johnston, *Chem. Rev.*, 2008, **108**, 845–910.

15352 | *Phys. Chem. Chem. Phys.*, 2023, **25**, 15340–15353

This journal is © the Owner Societies 2023

58 G. Krishnan, M. A. Verheijen, G. H. ten Brink, G. Palasantzas and B. J. Kooi, *Nanoscale*, 2013, **5**, 5375–5383.

59 Y. Li, N. M. Tam, P. Claes, A. P. Woodham, J. T. Lyon, V. T. Ngan, M. T. Nguyen, P. Lievens, A. Fielicke and E. Janssens, *J. Phys. Chem. A*, 2014, **118**, 8198–8203.

60 E. J. Baerends, V. Branchadell and M. Sodupe, *Chem. Phys. Lett.*, 1997, **265**, 481–489.

61 S. Pittalis, S. Kurth and E. K. U. Gross, *J. Chem. Phys.*, 2006, **125**, 084105.

62 Y. Chen, J. Yang and C. Dong, *Comput. Theor. Chem.*, 2019, **1170**, 112635.

63 Y. Chen, Y. Liu, S. Li and J. Yang, *J. Cluster Sci.*, 2019, **30**, 789–796.

64 N. A. Borshch, N. S. Pereslavtseva and S. I. Kurganskii, *J. Phys. Conf. Ser.*, 2019, **1203**, 012056.

65 C. Dong, L. Han, J. Yang and L. Cheng, *Int. J. Mol. Sci.*, 2019, **20**, 2933.

66 Y. Gu, J. Yang and L. Cheng, *Int. J. Quant. Chem.*, 2020, **120**, e26087.

67 Y. R. Zhao, T. T. Bai, L. N. Jia, W. Xin, Y. F. Hu, X. S. Zheng and S. T. Hou, *J. Phys. Chem. C*, 2019, **123**, 28561–28568.

68 L. V. Duong, N. N. Tri, N. P. Hung and M. T. Nguyen, *J. Phys. Chem. A*, 2022, **126**, 3101–3109.

69 S.-J. Lu, X.-L. Xu, G. Feng, H.-G. Xu and W.-J. Zheng, *J. Phys. Chem. C*, 2016, **120**, 25628–25637.

70 A. Shvartsburg, B. Liu, M. Jarrold and K.-M. Ho, *J. Chem. Phys.*, 2000, **112**, 4517–4526.

71 A. Zdetsis, *J. Chem. Phys.*, 2008, **127**, 244308.

72 S. Nigam, C. Majumder and S. K. Kulshreshtha, *J. Chem. Phys.*, 2004, **121**, 7756–7763.

73 N. M. Tam and M. T. Nguyen, *Chem. Phys. Lett.*, 2013, **584**, 147–154.

74 E. G. Lewars, in *Computational Chemistry: Introduction to the Theory and Applications of Molecular and Quantum Mechanics*, ed. E. G. Lewars, Springer International Publishing, Cham, 2016, pp. 9–49.

75 G. W. T. M. J. Frisch, H. B. Schlegel, G. E. Scuseria, M. A. Robb, J. R. Cheeseman, G. Scalmani, V. Barone, G. A. Petersson, H. Nakatsuji, X. Li, M. Caricato, A. Marenich, J. Bloino, *et al.*, *Gaussian 09, Rev. A.01*, Gaussian, Inc., Wallingford CT, 2009.

76 E. D. Glendening, J. K. Badenhoop, A. E. Reed, J. E. Carpenter, J. A. Bohmann, C. M. Morales and F. Weinhold, *Theoretical Chemistry Institute*, University of Wisconsin, Madison, WI, 2004.

77 J. He, K. Wu, C. Liu and R. Sa, *Chem. Phys. Lett.*, 2009, **483**, 30–34.

78 P. W. Atkins and J. De Paula, *Atkins' Physical Chemistry*, Oxford University Press, Oxford, 2014.

79 W. Ma, L. Xu, A. F. de Moura, X. Wu, H. Kuang, C. Xu and N. A. Kotov, *Chem. Rev.*, 2017, **117**, 8041–8093.

This journal is © the Owner Societies 2023

Phys. Chem. Chem. Phys., 2023, **25**, 15340–15353 | 15353